Science Advances
AAAS

advances.sciencemag.org/cgi/content/full/6/14/eaaz4888/DC1

Supplementary Materials for

Quantum biology revisited

Jianshu Cao, Richard J. Cogdell, David F. Coker, Hong-Guang Duan, Jürgen Hauer, Ulrich Kleinekathöfer, Thomas L. C. Jansen, Tomáš Mančal, R. J. Dwayne Miller*, Jennifer P. Ogilvie, Valentyn I. Prokhorenko, Thomas Renger, Howe-Siang Tan, Roel Tempelaar, Michael Thorwart, Erling Thyrhaug, Sebastian Westenhoff, Donatas Zigmantas

*Corresponding author. Email: dwayne.miller@mpsd.mpg.de

Published 3 April 2020, *Sci. Adv.* **6**, eaaz4888 (2020)
DOI: 10.1126/sciadv.aaz4888

The PDF file includes:

Other Supplementary Material for this manuscript includes the following:

(available at advances.sciencemag.org/cgi/content/full/6/14/eaaz4888/DC1)

Supplementary Text

section S1. Hamiltonian

The theory is based on the standard Frenkel exciton Hamiltonian

$$H = \sum_m \left(E_m + \sum_\xi \hbar\omega_\xi g_\xi^{(m)} Q_\xi \right) |m\rangle\langle m| + \sum_{m,n}^{m\neq n} V_{mn} |m\rangle\langle n| + \sum_\xi \frac{\hbar\omega_\xi}{4} \left(Q_\xi^2 + P_\xi^2 \right) , \tag{S1}$$

where $|m\rangle$ is a localized excited state of the complex, in which pigment m is excited and all other pigments are in their electronic ground state. The diagonal element E_m is the local electronic transition energy of pigment m at the equilibrium position of nuclei in the electronic ground state, termed site energy. The coupling constant $g_\xi^{(m)}$ describes how the site energy of pigment m fluctuates if the vibrational coordinates Q_ξ are displaced from their equilibrium positions. The off-diagonal element V_{mn} describes the coupling between localized excited states m and n (excitonic coupling). In principle, also the excitonic couplings are modulated by the vibrational dynamics of the complex. However, this modulation was found to be about two orders of magnitude smaller than that of the site energies and can, therefore, be neglected (*23*). The last part of the Hamiltonian describes the vibrational dynamics, where Q_ξ and P_ξ are dimensionless coordinates and momenta of vibrational mode ξ of the pigment-protein complex. A description in terms of (effective) harmonic oscillators is chosen.

A challenge for a theoretical description is the comparable magnitude of the excitonic and the exciton-vibrational coupling. The nearest neighbor excitonic couplings V_{mn} in the FMO protein and the exciton-vibrational reorganization energy

$$E_\lambda = \sum_\xi \hbar\omega_\xi g_\xi^2 \tag{S2}$$

of the local electronic transition of the pigments are in the same order of magnitude. E_λ is the energy released after optical excitation of a localized excited state of the complex, caused by relaxation of nuclei to a new equilibrium position. Electronic delocalization in a homo dimer lowers the excited state by the excitonic coupling V_{12} between the two monomers and by the reorganization energy of the low energy exciton state, which, however equals only half the reorganization energy of a localized excitation. Hence, there is a certain competition between the excitonic coupling and the exciton-vibrational coupling in the minimization of the free energy of excited states. Whereas the former lowers the free energy by delocalization, the latter does it by localization of excited states.

Transformation of the Hamiltonian in eq. (S1) to the basis of exciton states $|M\rangle = \sum_m c_m^{(M)} |m\rangle$, defined as the eigenstates of the above Hamiltonian at the equilibrium position of nuclei in the electronic ground state of the complex, gives

$$\begin{aligned} H &= \sum_M \left(E_M + \sum_\xi \hbar\omega_\xi g_\xi(M,M) Q_\xi \right) |M\rangle\langle M| + \sum_{M,N}^{M\neq N} \hbar\omega_\xi g_\xi(M,N) Q_\xi |M\rangle\langle N| \\ &+ \sum_\xi \frac{\hbar\omega_\xi}{4} \left(Q_\xi^2 + P_\xi^2 \right) , \end{aligned} \tag{S3}$$

with the exciton-vibrational coupling constant in the new basis reading

$$g_\xi(K,M) = \sum_m g_\xi^{(m)} c_m^{(K)} c_m^{(M)} . \tag{S4}$$

Due to the partial localization of exciton states, caused by the different site energies of the pigments, the off-diagonal elements $g_\xi(K,M)$ $(K \neq M)$ are smaller than the diagonal elements $g_\xi(M,M)$, as discussed in detail later, see Fig. S2 and the discussion below eq. (S9). This inequality will be used below, where an exact theory is used for the diagonal elements and the off-diagonal elements are treated in Markov and secular approximation.

section S2. Parameterization of the exciton-vibrational Hamiltonian

The site energies and excitonic couplings determined by Schmidt am Busch *et al.* (*17*) for the holo structure from *P. aestuarii* (*106*) are used. The numerical values are given in Table S1. The exciton-vibrational coupling is described by the spectral density

$$J(\omega) = \sum_\xi g_\xi^2 \delta(\omega - \omega_\xi)\,, \tag{S5}$$

that contains the square of the local coupling constant $g_\xi^{(m)}$ of the modulation of pigment transition energies from eq. (S1).

Note that we assume a site-independent spectral density for simplicity. In the present calculations the spectral density extracted from fluorescence line narrowing experiments on the FMO protein of *P. aestuarii* by Wendling *et al.* (*105*) is used (Fig. S1). The Huang Rhys factor $S = \int d\omega J(\omega)$ was extracted by the same authors from the temperature dependence of the low energy absorption band of the FMO protein, resulting in $S = 0.45$ (*105*). With this spectral density a reorganization energy of the local optical transition E_λ (eq. (S2)) of 45 cm^{-1} results, which is in the same order of magnitude as the excitonic couplings (Table S1).

We note that Wendling *et al.* (*105*) used a two-level system theory and, therefore, obtained an effective spectral density of the lowest exciton transition (*107*). However, since this transition is practically localized at a single pigment (*16*) (BChl 3, see Fig. 1D of the main text), it can be assumed that this spectral density is already very close to the local spectral density of this pigment. We will check this assumption and the above parameterization of the exciton Hamiltonian of the FMO protein by calculating various optical spectra using a multi-level theory, summarized next.

section S3. Theory of optical spectra and delocalization of excited states

The inequality between diagonal and off-diagonal exciton-vibrational coupling constants in the exciton basis (eq. (S4)) is used in the following, where an exact treatment of the diagonal elements is combined with a Markov and secular approximation for the off-diagonal elements. For this purpose we use a second-order cumulant expansion with partial ordering prescription (POP) (*104*). The lineshape of linear optical spectra is obtained from the off-diagonal density matrix elements ρ_{M0}, for which the equation of motion

$$\frac{\partial}{\partial t}\rho_{M0}(t) = -i\omega_{MO}\rho_{M0} - \sum_{KL}\gamma_{MKKL}\int_0^t d\tau C(\tau)e^{i\omega_{KL}\tau}\rho_{L0}(t) \tag{S6}$$

holds, where $C(t) = \int_0^\infty d\omega\omega^2 J(\omega)\left[(1+n(\omega))e^{-i\omega t} + n(\omega)e^{i\omega t}\right]$ is the correlation function of the fluctuations in the local transition energy of the pigments containing the Bose-Einstein distribution function of vibrational quanta $n(\omega)$ and the spectral density $J(\omega)$ of eq. (S5). The constant

$$\gamma_{MKKL} = \sum_m c_m^{(M)} c_m^{(K)} c_m^{(K)} c_m^{(L)} \tag{S7}$$

contains exciton coefficients and was obtained by assuming that the fluctuations in the site energies of different pigments are uncorrelated. Due to the off-diagonal elements $g_\xi(M,K)$ and $g_\xi(K,L)$ different off-diagonal elements of the density matrix ρ_{M0} and ρ_{L0} $(L \neq M)$ are coupled. These couplings to a minor extent can redistribute oscillator strength between different exciton states, but, in general, they do not have a significant effect on the linear optical spectra (*108, 109*). Applying a secular approximation to eq. (S6) restricts the sum over L on the r.h.s. to $L = M$. The solution of the resulting equation reads (*104, 110*)

$$\rho_{M0}(t) = \rho_{M0}(0) \exp\left\{ -i\omega_{M0}t - \sum_K \gamma_{MK} \int_0^t d\tau (t-\tau) C(\tau) e^{i\omega_{MK}\tau} \right\} , \tag{S8}$$

where

$$\gamma_{MK} \equiv \gamma_{MKKM} , \tag{S9}$$

which for $K \neq M$ contains the off-diagonal exciton vibrational coupling constants $g_\xi(M,K)$ and for $K = M$ the diagonal exciton vibrational coupling constants $g_\xi(M,M)$. The (disorder-averaged) diagonal and off-diagonal elements obtained for the FMO protein are compared in Fig. S2. The diagonal elements are indeed larger than the off-diagonal elements. This inequality is used to apply a Markov approximation to the off-diagonal elements, that is,

$$\gamma_{MK} \int_0^t d\tau (t-\tau) C(\tau) e^{i\omega_{MK}\tau} \approx \gamma_{MK} t \int_0^\infty d\tau C(\tau) e^{i\omega_{MK}\tau} = \gamma_{MK} t \tilde{C}(\omega_{MK}) \tag{S10}$$

for $(M \neq K)$. The real part of $\tilde{C}(\omega_{MK})$ is related to the spectral density $J(\omega)$ by

$$\tilde{C}^{\mathrm{Re}}(\omega) = \pi\omega^2 \left\{ [1+n(\omega)]J(\omega) + n(-\omega)J(-\omega) \right\} , \tag{S11}$$

and the imaginary part of $\tilde{C}(\omega_{MK})$ is obtained from the real part by the principal value integral

$$\tilde{C}^{\mathrm{Im}}(\omega) = \frac{1}{\pi} \wp \int_{-\infty}^{\infty} d\omega \frac{\tilde{C}^{\mathrm{Re}}(\omega)}{\omega_{MK} - \omega} . \tag{S12}$$

The diagonal elements of the exciton-vibrational coupling in eq. (S8) are treated exactly, yielding

$$\gamma_{MM} \int_0^t d\tau (t-\tau) C(\tau) = -\gamma_{MM} \left(G(t) - G(0) + i\frac{E_\lambda}{\hbar} t \right) , \tag{S13}$$

with the function

$$G(t) = \int_0^\infty d\omega J(\omega) \left\{ [1+n(\omega)] e^{-i\omega t} + n(\omega) e^{i\omega t} \right\} , \tag{S14}$$

and the reorganization energy E_λ of the local electronic transitions as defined in eq. (S2). The linear absorption spectrum is determined by the half-sided Fourier transform of the dipole-dipole correlation function $\alpha(\omega) \propto \omega \mathrm{Re} \int_0^\infty dt e^{i\omega t} D(t)$, which is given by $D(t) = \sum_M \mu_{M0}\mu_{0M}(t)$, with $\mu_{0M}(t) = \mu_{0M}\rho_{M0}(t)$ with the above $\rho_{M0}(t)$ and $\rho_{M0}(0) = 1$, resulting in

$$\alpha(\omega) \propto \omega \sum_M |\mu_{M0}|^2 D_M(\omega) , \tag{S15}$$

with the lineshape function

$$D_M(\omega) = \frac{1}{2\pi} \int_{-\infty}^{\infty} dt e^{i(\omega - \tilde{\omega}_{M0})t} e^{\gamma_{MM}\{G(t)-G(0)\}} e^{-|t|/\tau_M} \tag{S16}$$

of the excitation of the Mth exciton state (*107*), where

$$\tilde{\omega}_{M0} = \omega_{M0} - \gamma_{MM} E_\lambda/\hbar + \sum_{K}^{K\neq M} \tilde{C}^{\mathrm{Im}}(\omega_{MK})\,, \tag{S17}$$

and the exciton relaxation-induced lifetime broadening

$$\tau_M^{-1} = \frac{1}{2}\sum_K k_{M\to K}\,, \tag{S18}$$

that contains the Redfield relaxation rate constant

$$k_{M\to K} = 2\gamma_{MK}\tilde{C}^{\mathrm{Re}}(\omega_{MK})\,, \tag{S19}$$

with the $\tilde{C}^{\mathrm{Re}}(\omega_{MK})$ given in eq. (S11). The prefactor γ_{MK} in eqs. (S7) and (S9) is a measure of the spatial overlap between the exciton states $|M\rangle$ and $|K\rangle$.
The linear dichroism spectrum $LD(\omega)$ is obtained by replacing the $|\mu_{M0}|^2$ in eq. (S15) by $|\mu_{M0}|^2(1-3\cos^2\theta_M)$, with the angle θ_M between the exciton transition dipole moment $\vec{\mu}_{M0}$ and the symmetry axis of the FMO trimer. In the calculation of the circular dichroism spectrum $CD(\omega)$, the $|\mu_{M0}|^2$ in eq. (S15) has to be replaced by $\sum_{m,n} c_m^{(M)} c_n^{(M)} \vec{R}_{mn}\cdot(\vec{\mu}_{m0}\times\vec{\mu}_{n0})$, with the distance vector $\vec{R}_{mn} = \vec{R}_m - \vec{R}_n$ and the local transition dipole moments $\vec{\mu}_{m0}$ and $\vec{\mu}_{n0}$ of pigments m and n, respectively.

Static disorder, caused by conformational motion that is slow compared to the excited state lifetimes, is considered by including distribution functions of site energies that are centered around the mean values given in Table S1. Motivated by the central limit theorem of statistical mechanics, a Gaussian functional form is assumed for these distribution functions. As reported in Ref. (*15*), the fit of the spectra can be somewhat improved by assigning a larger width to the distribution functions of those pigments which are in contact with water molecules. Based on this criterion, a FWHM of 60 cm^{-1} was assigned for BChls 1, 3 and 4, 100 cm^{-1} for BChl 2, and 120 cm^{-1} for BChls 5 - 7 (*15*). We take the same values in the present calculations. In the calculation of the spectra, the site energy is randomly chosen from each distribution function, and for this particular realization of static disorder a homogeneous spectrum is calculated. The inhomogeneous spectrum is obtained as an average over many (30000) such realizations. The linear optical spectra (absorption, linear and circular dichroism), obtained with the above theory and parameters, are compared to experimental data (*105, 111*) in Fig. S3 revealing a good quantitative agreement. From the agreement of the temperature dependence of the absorption spectrum (right half of Fig. S3), we conclude that the effective spectral density extracted by Wendling *et al.* (*105*) for the lowest exciton state is close to the local spectral density of the pigments. In order to further improve the agreement between experimental and calculated spectra, it will be helpful to (i) refine the parameterization of the exciton Hamiltonian by, e.g., including a site-specific spectral density of the local pigment-protein coupling, and/or (ii) to include non-secular and non-Markovian effects in the treatment of off-diagonal elements of the exciton-vibrational coupling in the theory of optical spectra (*108-110*).

In order to visualize the delocalization of excited states in energy, we compare the density of exciton states $d_M(\omega)$, defined as

$$d_M(\omega) = \left\langle \sum_M \delta(\omega-\omega_{M0}) \right\rangle_{\mathrm{dis}}\,, \tag{S20}$$

with the exciton states pigment distribution function (*112*)

$$d_m(\omega) = \left\langle \sum_M |c_m^{(M)}|^2 \delta(\omega-\omega_{M0}) \right\rangle_{\mathrm{dis}}\,, \tag{S21}$$

where the sums run over all exciton states $|M\rangle$. Moreover, $|c_m^{(M)}|^2$ is the probability to find pigment m excited in the exciton state $|M\rangle$, and $\langle ...\rangle_{\rm dis}$ denotes an average over static disorder in the site energies. The functions $d_M(\omega)$ and $d_m(\omega)$ resulting from the above parameterization of the exciton Hamiltonian are compared in Fig. 1D of the main text. As seen there, the lowest exciton state is strongly localized at BChl 3 with a minor contribution from BChl 4, the second exciton state has the largest contribution from BChl 4 and some minor contributions from BChls 3, 5-7. The third and the sixth exciton states are delocalized over BChls 1 and 2 and the 4th and 5th exciton state are delocalized over BChls 4-7. The seventh exciton state is delocalized over pigments 5 and 6. The highest exciton state is mainly localized at BChl 8 with a minor contribution from BChl 1. A structural illustration of the delocalization of exciton states is given in Fig. 1A of the main text, where the 8 BChl pigments of the monomeric subunit of the FMO protein are shown in an orientation, in which the baseplate is situated above and the reaction center complex below the FMO protein and those pigments, that contribute to a certain exciton state, are enclosed by lines. The high-energy exciton states 1 and 2 (blue lines) formed by BChls 8 and 1 and by BChls 5 and 6 are situated in the upper part of the FMO protein, that is close to the baseplate, from where the excitation energy arrives. The central part contains intermediate-energy exciton states 3-7 (green lines) with contributions from BChls 1,2, 4-7 and the lowest-energy exciton state 7 (red line) is situated at the bottom of the complex close to the reaction center.

Finally, we note that the inequality between the diagonal and off-diagonal exciton-vibrational coupling constants γ_{MN} (Fig. S2) ensures that the delocalization of excitons is limited by the difference in site energies and not by the exciton-vibrational coupling. In other words, the dynamic localization of excitons is small in the FMO protein.

section S4. Exciton relaxation and decay of coherences after δ-pulse excitation

Within second-order perturbation theory in the coupling of the complex with an external δ-pulse $\vec{E}(t) = A\vec{e}\delta(t)$, with amplitude A and polarization unit vector $\vec{e}$, the initial exciton density matrix $\rho_{MN}(0)$ is obtained as

$$\begin{aligned} \rho_{MN}(0) &= \frac{2A^2}{\hbar^2}\langle(\vec{e}\cdot\vec{\mu}_M)(\vec{e}\cdot\vec{\mu}_N)\rangle_{\rm orient} \\ &= \frac{2A^2}{3\hbar^2}\mu_M\mu_N\cos\alpha_{MN}\,, \end{aligned} \tag{S22}$$

where $\langle ...\rangle_{\rm orient}$ denotes an orientational average over randomly oriented complexes in the sample and α_{MN} is the angle between the exciton transition dipole moments $\vec{\mu}_M$ and $\vec{\mu}_N$. In secular approximation, the dissipative dynamics of the exciton state populations ρ_{MM} and of the coherences between exciton states are decoupled. The population dynamics is described by the master equation

$$\frac{\partial}{\partial t}\rho_{MM}(t) = -\sum_K^{K\neq M}\left\{k_{M\to K}\rho_{MM}(t) - k_{K\to M}\rho_{KK}(t)\right\}\,, \tag{S23}$$

with the Redfield rate constant $k_{M\to K}$ given in eqs. (S11) and (S19). The evolution of exciton coherences in secular approximation is obtained from (*23*)

$$\frac{\partial}{\partial t}\rho_{MN}(t) = -(i\omega_{MN} + F_{MN}(t))\rho_{MN}(t)\,, \tag{S24}$$

with the time-dependent function

$$F_{MN}(t) = \sum_L\int_0^t d\tau\left[\gamma_{ML}e^{i\omega_{ML}\tau}C(\tau) + \gamma_{NL}e^{i\omega_{LN}\tau}C^*(\tau)\right] - 2\gamma_{MMNN}\Re\int_0^t d\tau C(\tau)\,, \tag{S25}$$

with the γ_{MMNN} and the γ_{MN} in given eqs. (S7) and (S9). Using again a Markov approximation for the off-diagonal elements of the exciton-vibrational coupling and integrating eq. (S24), we obtain

$$\begin{aligned}\rho_{MN}(t) &= \rho_{MN}(0)e^{-i\tilde{\omega}_{MN}t}e^{-t(1/\tau_M+1/\tau_N)}e^{\gamma_{MM}(G(t)-G(0))}e^{\gamma_{NN}(G^*(t)-G(0))} \\ &\times \; e^{-\gamma_{MMNN}(G(t)+G^*(t)-2G(0))}\,.\end{aligned}$$

Within a short-time approximation for the temperature-independent imaginary part of $G(t)$, that shifts the exciton state energies, we obtain

$$\rho_{MN}(t) = \rho_{MN}(0)e^{-i\omega'_{MN}t}\Gamma_{MN}(t)\,, \tag{S26}$$

with the damping function

$$\Gamma_{MN}(t) = e^{\kappa_{MN}\{G^{\mathrm{Re}}(t)-G(0)\}}e^{-t(1/\tau_M+1/\tau_N)}\,, \tag{S27}$$

where

$$\kappa_{MN} = \gamma_{MM} + \gamma_{NN} - 2\gamma_{MN} = \sum_m \left(|c_m^{(M)}|^2 - |c_m^{(N)}|^2\right)^2\,, \tag{S28}$$

and

$$\omega'_{MN} = \omega_{MN} + \sum_K^{K\neq M}\gamma_{MK}\tilde{C}^{\mathrm{Im}}(\omega_{MK}) - \sum_K^{K\neq N}\gamma_{NK}\tilde{C}^{\mathrm{Im}}(\omega_{NK})\,. \tag{S29}$$

As described above (see section on the linear absorption), the coherence between the electronic ground state and the Mth exciton state is given as

$$\begin{aligned}\rho_{M0}(t) &= \rho_{M0}(0)e^{-i\omega'_{M0}t}e^{\gamma_{MM}\{G^{\mathrm{Re}}(t)-G(0)\}}e^{-t/\tau_M} \\ &= \rho_{M0}(0)e^{-i\omega'_{M0}t}\Gamma_{M0}(t)\,,\end{aligned} \tag{S30}$$

where a short-time approximation was used for the imaginary part of $G(t)$, see eq. (S14) shifting the exciton energies. Moreover, the damping function

$$\Gamma_{M0}(t) = e^{\gamma_{MM}\{G^{\mathrm{Re}}(t)-G(0)\}}e^{-t/\tau_M} \tag{S31}$$

was introduced, containing the real part of $G(t)$ and the exciton relaxation-induced life time broadening constants τ_M, see eq. (S18). The frequency ω'_{M0} reads

$$\omega'_{M0} = \omega_{M0} + \sum_K^{K\neq M}\gamma_{MK}\tilde{C}^{\mathrm{Im}}(\omega_{MK})\,, \tag{S32}$$

with the $\tilde{C}^{\mathrm{Im}}(\omega_{MK})$ given in eq. (S12).

As shown in section S6 below, a classical treatment of the nuclear motion results in a function $G(t) = 2k_{\mathrm{B}}T\int_0^\infty \frac{J(\omega)}{\hbar\omega}\cos(\omega t)$. Applying, in addition, a short time approximation to the cos function ($\cos(\omega t) \approx 1 - \frac{\omega^2 t^2}{2}$) leads to the classical limit

$$\rho^{\mathrm{cl}}_{MN}(t) = \rho_{MN}(0)e^{-i\omega'_{MN}t}\Gamma_{MN}(t) \tag{S33}$$

of the evolution of inter-exciton coherences, with the classical damping function

$$\Gamma_{MN}(t) = \exp\left[-(1/\tau_M^{\mathrm{cl}} + 1/\tau_N^{\mathrm{cl}})t - \kappa_{MN}\frac{E_\lambda k_{\mathrm{B}}T}{\hbar^2}t^2\right]\,, \tag{S34}$$

with

$$1/\tau_M^{\rm cl} = \frac{1}{2}\sum_K k_{M\to K}^{\rm (cl)}\,, \tag{S35}$$

which contains the classical limit of the Redfield rate constant, obtained in section S6 as

$$k_{M\to K}^{\rm (cl)} = \frac{2\pi k_{\rm B}T}{\hbar}\gamma_{MK}|\omega_{MK}|J(|\omega_{MK}|) = k_{K\to M}^{\rm (cl)}\,. \tag{S36}$$

We note that in this limit the exact form of the detailed balance condition $k_{M\to K}/k_{K\to M} = \exp(\hbar\omega_{MN}/k_{\rm B}T)$ is not fulfilled. It is only fulfilled in the high-temperature limit $k_{\rm B}T \gg \hbar\omega_{MN}$. As discussed in section S6, the neglect of the quantum mechanical uncertainty principle is responsible for this result.

The classical limit of the damping function $\Gamma_{M0}(t)$ of the coherence between the ground state and the Mth exciton state, see eq. (S31), is obtained similarly as

$$\Gamma_{M0}(t) = \exp(-t/\tau_M)\exp\left(-\Lambda_M\frac{E_\lambda k_{\rm B}T}{\hbar^2}t^2\right)\,, \tag{S37}$$

with the inverse participation ratio

$$\Lambda_M = \gamma_{MM} = \sum_m |c_m^{(M)}|^4 \tag{S38}$$

of the Mth exciton state.

The populations of local excited states follow from the above exciton density matrix and the coefficients of the exciton states as

$$P_m(t) = \sum_{M,N} c_m^{(M)} c_m^{(N)} \rho_{MN}(t)\,. \tag{S39}$$

A similar relation holds for the classical populations $P_m^{\rm cl}(t) = \sum_{M,N} c_m^{(M)} c_m^{(N)} \rho_{MN}^{\rm cl}(t)$, where the classical off-diagonal elements are given in eq. (S33) and the classical diagonal elements are obtained by solving eq. (S23) with the classical rate constants $k_{M\to K}^{\rm (cl)}$ in eq. (S36).

The disorder-averaged exciton dynamics initiated by δ-pulse excitation at 300 K is shown in Fig. S4, where we compare the exciton state populations and the populations of local excited states obtained by using a quantum mechanical description of nuclear motion with the classical limit, see eq. (S36), described above. The violation of the detailed balance condition for the classical rate constants has a dramatic effect on the equilibrium populations of exciton states and local excited states, which in the classical limit are equal for all exciton states and all pigments. In contrast, the quantum mechanical description leads to a correct Boltzmann population of exciton states. Since the exciton states are partially localized at certain pigments, also the equilibrium population of local excited states is different. BChl 3, which has the largest contribution in the lowest exciton state, is populated strongest after exciton relaxation. Please note that the FMO protein is indeed oriented such, as predicted theoretically (*19*) and proven experimentally (*20*), that BChl 3 is closest to the reaction center complex, the final destination of the excitation energy.

The inter-exciton coherences ρ_{MN} are shown together with the corresponding damping functions $\Gamma_{MN}(t)$ in Fig. 1E of the main text. Both, in a classical and in a quantum description these coherences decay in about 50 fs, at room temperature. This decay is somewhat faster than that of the coherences ρ_{M0} between the exciton states and the ground state occurring in about 75 fs, as shown in Fig. 1F in the main text. In both cases the damping is dominated by pure dephasing

processes, which in the classical limit contribute a factor $\exp\left(-\kappa_{MN}\frac{E_\lambda k_B T}{\hbar^2}t^2\right)$ to the damping of inter-exciton coherences and a factor $\exp\left(-\Lambda_M\frac{E_\lambda k_B T}{\hbar^2}t^2\right)$ to that of optical coherences. Due to the partial localization of exciton states in FMO, it holds that $\kappa_{MN} > \Lambda_M$ and, hence, inter-exciton coherences decay somewhat faster.

It is interesting to note that the population dynamics (Fig. S4) is much more influenced by quantum effects in the nuclear motion than the decay of inter-exciton and optical coherences (Fig. 1E in the main text), simply because of the classical violation of the detailed balance principle. Please note, that there are semiclassical approaches in the literature that are able to circumvent this deficiency by taking into account the reaction of the quantum (electronic degrees of freedom) part on the classical (vibrational degrees of freedom) part of the system in an appropriate way (*113*). It might even be possible to go one step further and describe the motion of the electronic and vibrational degrees of freedom classically, but "quantizing" the action variables of the electronic motion by histogram "window functions" (*114*).

From a more fundamental point of view it is the quantum mechanical uncertainty principle for the spatial coordinates and momenta of the electrons and nuclei that is responsible for the directed energy transfer. If there was no uncertainty for electrons, there would be no discrete excited states and if there was no uncertainty for nuclei, there would be no preference for the population of low energy excited states of the electrons (see section S6).

Transformation of the exciton density matrix to the local basis gives

$$\rho_{mn} = \sum_{M,N} c_m^{(M)} c_n^{(N)} \rho_{MN}(t)\,, \tag{S40}$$

where the off-diagonal elements $m \neq n$ contain the spatial coherences between different pigments m and n. The inter-pigment coherences, resulting at $T = 300$ K for a δ-pulse excitation at time zero (as before) are shown in Fig. S5. After some initial fast decaying oscillations (caused by the inter-exciton coherences created by the δ-pulse excitation), the inter-pigment coherences relax towards their non-zero equilibrium values, which reflect the delocalization of Boltzmann populated exciton states. The non-zero equilibrium values of inter-pigment coherences demonstrate that the site basis is not suitable for an interpretation of optical spectroscopy. The latter always detects the eigenstates of a system, that can be identified as the basis, in which the equilibrium off-diagonal elements of the density matrix become zero.

section S5. Exciton relaxation initiated by incoherent transfer from the baseplate

The excitation energy transfer from the baseplate is described by generalized Förster theory, where we take into account the partial localization of exciton states in the FMO protein and the knowledge about the polarization and the optical lineshape of the low-energy excited state of the baseplate (*115*). The initial conditions of exciton populations in the FMO protein are chosen according to the rate constants $k_{b\to M}$ for the transfer from the baseplate to the respective exciton state, $\rho_{MM}(0) \propto k_{b\to M}$, which in generalized Förster theory reads (*9*)

$$k_{b\to M} \propto |V_{bM}|^2 \int d\omega D'_b(\omega) D_M(\omega)\,, \tag{S41}$$

where $|V_{bM}|^2$ is the electronic coupling between the transition density of the low-energy state of the baseplate and that of the Mth exciton state in the FMO protein and $D'_b(\omega)$ and $D_M(\omega)$ are the fluorescence lineshape functions of the low energy baseplate state and the absorption lineshape function of the Mth exciton state in the FMO protein, respectively. Taking into account that

the low-energy state of the baseplate is polarized in the plane of the baseplate (*115*), that is perpendicular to the symmetry axis $\vec{e}$ of the FMO protein, and that the exciton states in the FMO protein are partially localized at neighboring pigments (*19*) (Figs. 1A and 1D of the main text) exhibiting a different distance to the baseplate, we estimate that

$$V_{bM} \propto \frac{\sin\theta_M}{(R_0 + \Delta R_M)^3}\,, \tag{S42}$$

where θ_M is the angle between the symmetry axis $\vec{e}$ of the FMO complex and the transition dipole moment $\vec{\mu}_M$ of the Mth exciton state, R_0 is the vertical distance between the baseplate plane and the center $\vec{R}_8$ of BChl 8 of the FMO protein and $\Delta R_M = \left(\sum_m^{|c_m^{(M)}|>0.3} \vec{R}_m - \vec{R}_8\right)\cdot\vec{e}$ corrects for different spatial localizations of exciton states giving rise to different vertical distances $R_0+\Delta R_M$ to the baseplate. $\vec{R}_m$ is the center of BChl m and the sum in ΔR_M runs only over those pigments that have an exciton coefficient with an absolute magnitude larger than 0.3 to exciton state $|M\rangle$. The lineshape function $D_M(\omega)$ in eq. (S16) is applied together with the parameters of the Hamiltonian outlined above. For the fluorescence lineshape function of the baseplate we use the analytical two-level system result (*116*)

$$D_b'(\omega) = \frac{1}{2\pi}\int_{-\infty}^{\infty} dt e^{-i(\omega-\omega_{b0})t} e^{G_b(t)-G_b(0)}\,, \tag{S43}$$

together with parameters estimated on the basis of a comparison with a recent analysis of absorption, linear and circular dichroism and anisotropic circular dichroism data (*115*), resulting in a transition energy $\hbar\omega_{b0}$ of 12422 cm^{-1} (corresponding to a wavelength $\lambda_{\mathrm{BP}} = 805$ nm) and a function $G_b(t) = G(t)$ in eq. (S43) calculated with the spectral density $J(\omega)$ that has the same functional form as that of the B777-complex (*104*) and a Huang-Rhys factor of 1.7. For the FWHM of the distribution function of the transition energy we obtain 283 cm^{-1}. These parameters have been estimated from a recent exciton model of the baseplate (*115*), taking into account the effect of the excitonic coupling on the excitation energies, the exciton-vibrational coupling and the width of the static distribution function of excitation energies.

The exciton dynamics calculated for $T = 300$ K is shown in Fig. S6 and compared again to the classical limit. Similar relaxation times as for the δ-pulse excitation (Fig. S4) are obtained. Initially, mainly the highest exciton state, which has the largest contribution from BChl 8 and therefore the closest distance to the baseplate, is excited. Equilibrium is reached in about 1.5 ps in both the quantum and the classical description of nuclear motion, with the deficiency of the classical population discussed above. A structural illustration of this deficiency is given in Fig. S8, where it becomes obvious that only a quantum mechanical description of nuclear motion leads to a directed energy transfer.

The relative pathways of exciton relaxation are relatively insensitive with respect to the exact values of the energy of the low-energy excited state of the baseplate and the vertical distance between BChl 8 and the baseplate plane, as demonstrated in Fig. S7, where the exciton relaxation for the above parameters ($\lambda_{\mathrm{BP}} = 805$ nm, $R_0 = 20$ Å) are compared to results obtained for $\lambda_{\mathrm{BP}} = 815$ and 825 nm (*117*) and $R_0 = 15$ and 25 Å, using a quantum mechanical treatment of the nuclear motion.

Since the transfer from the baseplate most likely takes much longer than the intra FMO equilibration time, only the relaxed state is relevant for the overall energy transfer process from the baseplate to the reaction center complex. An explicit inclusion of the baseplate-to-FMO transfer has to await better defined structural information.

section S6. Classical description of the nuclear motion

Nuclear motion enters the above theories only in the correlation function $C(t)$ of the local energy gap of the pigments, which will be calculated classically in the following. For this purpose, we rewrite the Hamiltonian in eq. (S1) using the completeness relation as

$$\begin{aligned} H &= \sum_m \left(E_m + \sum_\xi \hbar\omega_\xi g_\xi^{(m)} Q_\xi \right) |m\rangle\langle m| + \sum_{m,n}^{m\neq n} V_{mn} |m\rangle\langle n| \\ &+ \sum_\xi \frac{\hbar\omega_\xi}{4} \left(Q_\xi^2 + P_\xi^2\right) \left(|0\rangle\langle 0| + \sum_m |m\rangle\langle m| \right) . \end{aligned} \tag{S44}$$

The energy gap between the mth localized excited state and the ground state is obtained from the diagonal elements of the above Hamiltonian as

$$X_m(t) = E_m + \sum_\xi \hbar\omega_\xi g_\xi^{(m)} Q_\xi(t) \, . \tag{S45}$$

Since we assume the same local coupling constants $g_\xi^{(m)}$ of all pigments, we can drop the index m in the following. Changing back from the dimensionless coordinates $Q_\xi(t)$ and momenta $P_\xi(t)$ to the original coordinates and momenta $q_\xi = Q_\xi/\sqrt{2\omega_\xi\mu_\xi/\hbar}$ and p_ξ with the reduced mass μ_ξ and the frequency ω_ξ of the ξth normal mode results in

$$X_m(t) = E_m + \sum_\xi \omega_\xi g_\xi \sqrt{2\hbar\omega_\xi\mu_\xi}\, q_\xi(t) \, , \tag{S46}$$

and a vibrational Hamiltonian of the electronic ground state

$$H_{\rm vib} = \sum_\xi \left(\frac{p_\xi^2}{2\mu_\xi} + \frac{\mu_\xi\omega_\xi^2}{2} q_\xi^2 \right) . \tag{S47}$$

The correlation function of the electronic energy gap of the pigments is defined as

$$C(t) = \frac{1}{\hbar^2} \langle \delta X(t) \delta X(0) \rangle \, , \tag{S48}$$

where

$$\delta X(t) = X(t) - \langle X \rangle \, . \tag{S49}$$

Here $\langle ... \rangle$ denotes an ensemble average with respect to Boltzmann distributed initial coordinates and momenta, defined below, and the time dependence of the energy gap is determined by $H_{\rm vib}$ given in eq. (S47). With eq. (S46) we obtain

$$\delta X(t) = \sum_\xi \omega_\xi g_\xi \sqrt{2\hbar\omega_\xi\mu_\xi}\, \left(q_\xi(t) - \langle q_\xi(t) \rangle \right) \, , \tag{S50}$$

where the time dependence of the coordinates $q_\xi(t)$ and momenta $p_\xi(t)$ is determined by Hamilton's classical canonical equations of motion

$$\dot{q_\xi} = \frac{\partial}{\partial p_\xi} H_{\rm vib} = \frac{p_\xi}{\mu_\xi} \tag{S51}$$

and

$$\dot{p_\xi} = -\frac{\partial}{\partial q_\xi} H_{\rm vib} = -\mu_\xi\omega_\xi^2 q_\xi \, , \tag{S52}$$

which are solved by

$$q_\xi(t) = q_{0\xi}\cos(\omega_\xi t) + \frac{p_{0\xi}}{\mu_\xi\omega_\xi}\sin(\omega_\xi t)\,, \tag{S53}$$

where $q_{0\xi} = q_\xi(t=0)$ and $p_{0\xi} = p_\xi(t=0)$ are the initial values of the coordinates and momenta. In the canonical ensemble, the initial momenta and coordinates are Boltzmann distributed and the ensemble average $\langle q_\xi(t)\rangle$ vanishes because

$$\langle q_{0\xi}\rangle \propto \int_{-\infty}^{+\infty} dq_{0\xi}\, q_{0\xi} e^{-\frac{\mu_\xi\omega_\xi^2}{2k_\mathrm{B}T}q_{0\xi}^2} = 0\,, \tag{S54}$$

and

$$\langle p_{0\xi}\rangle \propto \int_{-\infty}^{+\infty} dp_{0\xi}\, p_{0\xi} e^{-\frac{p_{0\xi}^2}{2\mu_\xi k_\mathrm{B}T}} = 0\,. \tag{S55}$$

The correlation function, therefore, becomes

$$\begin{aligned} C(t) &= \frac{2}{\hbar}\sum_\xi \omega_\xi^3\mu_\xi g_\xi^2\langle q_\xi(t)q_{0\xi}\rangle \\ &= \frac{2}{\hbar}\sum_\xi \omega_\xi^3\mu_\xi g_\xi^2\left(\cos(\omega_\xi t)\langle q_{0\xi}^2\rangle + \sin(\omega_\xi t)\langle q_{0\xi}p_{0\xi}\rangle\right)\,. \end{aligned} \tag{S56}$$

Since the expectation value $\langle q_{0\xi}p_{0\xi}\rangle$ factorizes, reflecting the fact that in classical physics there is no correlation between initial coordinates and momenta, we have, using eqs. (S54) and (S55), that

$$C(t) = \frac{2}{\hbar}\sum_\xi \omega_\xi^3\mu_\xi g_\xi^2\cos(\omega_\xi t)\langle q_{0\xi}^2\rangle\,. \tag{S57}$$

The ensemble average on the r.h.s. is obtained as

$$\langle q_{0\xi}^2\rangle = \frac{\int_{-\infty}^{+\infty} dq_{0\xi}\, q_{0\xi}^2 e^{-\frac{\mu_\xi\omega_\xi^2}{2k_\mathrm{B}T}q_{0\xi}^2}}{\int_{-\infty}^{+\infty} dq_{0\xi}\, e^{-\frac{\mu_\xi\omega_\xi^2}{2k_\mathrm{B}T}q_{0\xi}^2}} = \frac{k_\mathrm{B}T}{\mu_\xi\omega_\xi^2}\,, \tag{S58}$$

and hence the classical correlation function reads

$$C(t) = \frac{2k_\mathrm{B}T}{\hbar}\sum_\xi \omega_\xi g_\xi^2\cos(\omega_\xi t)\,. \tag{S59}$$

The exciton relaxation rate constant $k_{M\to K}$ in eq. (S19) is obtained from the real part of the half-sided Fourier transform of the correlation function $\tilde{C}^{\mathrm{Re}}(\omega=\omega_{MK})$, which is obtained as

$$\begin{aligned} \tilde{C}^{\mathrm{Re}}(\omega) &= \frac{1}{2}\int_0^\infty dt\left[e^{i\omega t}C(t) + e^{-i\omega t}C^*(t)\right] \\ &= \frac{1}{2}\int_{-\infty}^\infty dt e^{i\omega t}C(t) \\ &= \frac{\pi k_\mathrm{B}T}{\hbar}\sum_\xi \omega_\xi g_\xi^2\left[\delta(\omega-\omega_\xi)+\delta(\omega+\omega_\xi)\right]\,. \end{aligned} \tag{S60}$$

Inserting this expression into eq. (S19) gives for the rate constant

$$k_{M\to K} = \frac{2\pi k_\mathrm{B}T}{\hbar}\gamma_{MK}\sum_\xi \omega_\xi g_\xi^2\left[\delta(\omega_{MK}-\omega_\xi)+\delta(\omega_{MK}+\omega_\xi)\right]\,, \tag{S61}$$

where ω_{MK} is the transition frequency between the Mth and the Kth exciton state. We note already that obviously the rate constant $k_{M\to K}$ equals $k_{K\to M}$ and hence the detailed balance principle obtained for a quantum mechanical treatment of nuclear motion does not hold. With the help of the spectral density $J(\omega)$ in eq. (S5), the above classical rate constant may be written as

$$k_{M\to K} = \frac{2\pi k_{\mathrm{B}}T}{\hbar}\gamma_{MK}|\omega_{MK}|J(|\omega_{MK}|)\,, \tag{S62}$$

which exactly equals the high-temperature limit of the quantum rate constant, see eqs. (S11) and (S19), while using $1+n(\omega)\approx n(\omega)\approx k_{\mathrm{B}}T/\hbar\omega$. Note, however, that the classical rate constant derived above does not fulfil detailed balance at any finite temperature. It is the neglect of the uncertainty principle in classical physics that leads to uncorrelated initial momenta and coordinates $\langle q_{0\xi}p_{0\xi}\rangle = 0$ and thereby to a time-symmetric real valued correlation function of the energy gap of the pigments that cannot describe the detailed balance of the rate constant of excitation energy transfer. The consequences of this violation are seen in the population dynamics of the exciton states and the local excited states in Figs. S4 and S6. An illustration of the local populations, assuming incoherent transfer from the baseplate, for a quantum and a classical description of nuclear motion is presented in Fig. S8. In a quantum description the detailed balance condition for the rate constant leads to a large equilibrium population of the lowest exciton state, located at the bottom. In a classical model no such directed energy transfer is obtained.

According to eq. (S13), the function $G(t)$ needed for the description of pure dephasing in the classical limit (real $C(t)$) is obtained as

$$\int_0^t d\tau(t-\tau)C(\tau) = -(G(t)-G(0))\,. \tag{S63}$$

With the $C(t)$ in eq. (S59) we obtain

$$G(t) = 2\sum_{\xi}\frac{k_{\mathrm{B}}T}{\hbar\omega_{\xi}}\cos(\omega_{\xi}t) = 2\int_0^{\infty} d\omega\frac{k_{\mathrm{B}}T}{\hbar\omega}J(\omega)\cos(\omega t)\,, \tag{S64}$$

which is used to derive the classical limit of the damping functions of the inter-exciton and optical coherences in eqs. (S27) and (S31), respectively. Interestingly, the classical damping functions provide a qualitatively correct description of the quantum results (Figs. 1E and 1F of the main text).

fig. S1. Spectral density of the FMO protein. Spectral density $J(\omega)$ extracted from fluorescence line-narrowing and temperature-dependent absorption data by Wendling *et al.* (*105*).

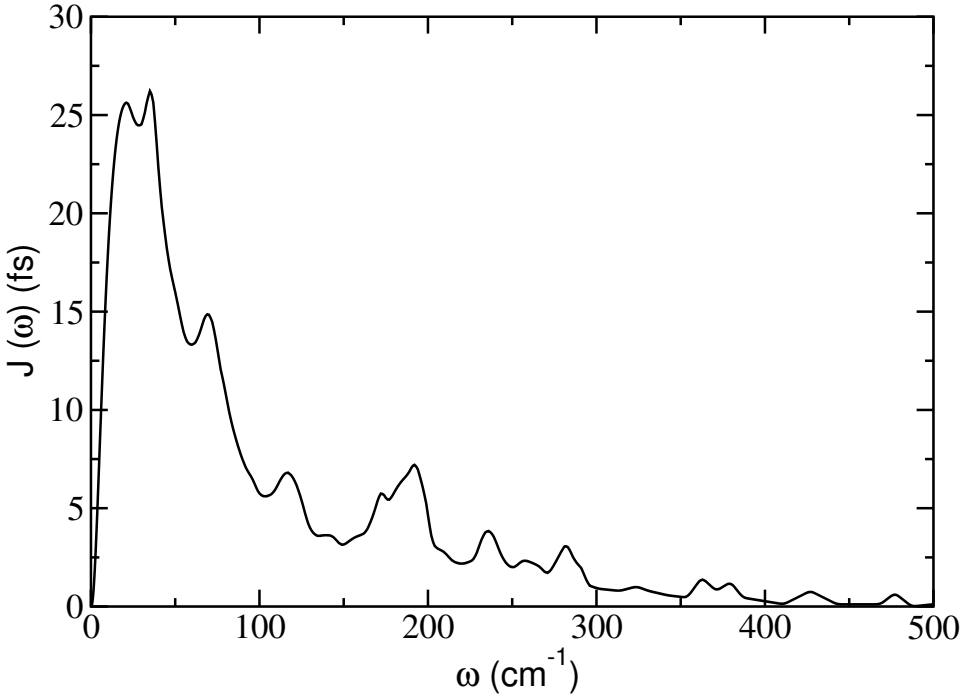

fig. S2. Matrix elements of the exciton-vibrational coupling of the FMO protein. Disorder-averaged elements γ_{MK} of eqs. (S7) and (S9) of the exciton-vibrational coupling. The horizontal dashed line is drawn between the diagonal elements in the upper and the off-diagonal elements in the lower part.

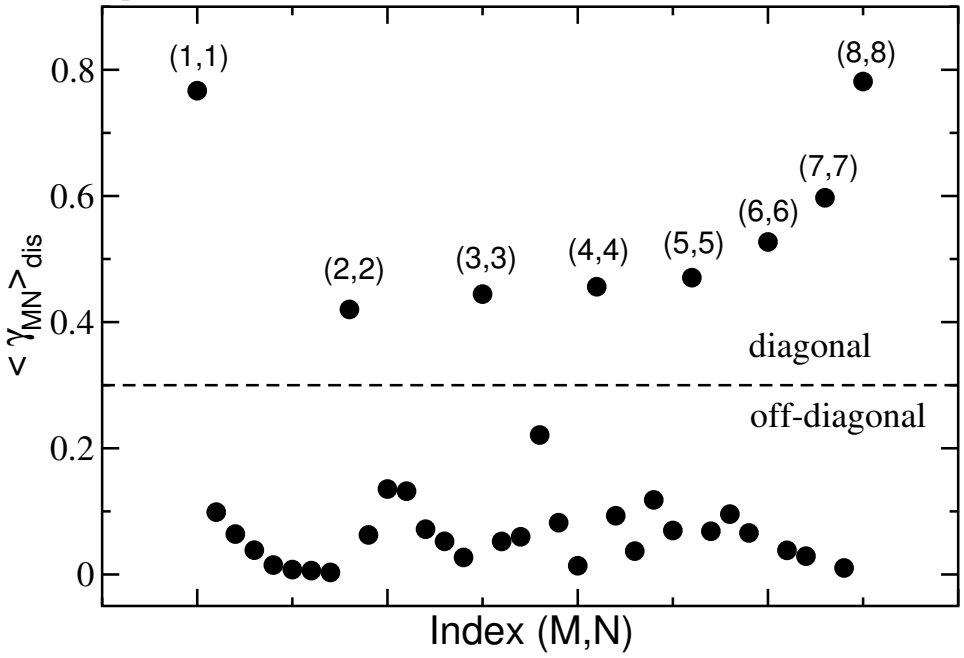

fig. S3. Linear optical spectra of the FMO protein. *Left*: Low temperature absorption (top), linear dichroism (middle) and circular dichroism spectra (bottom). Calculations (solid lines) are compared with experimental data (*111*) (dashed lines). *Right*: Temperature dependence of linear absorption. The upper part contains the experimental (*105*) and the lower part the calculated spectra.

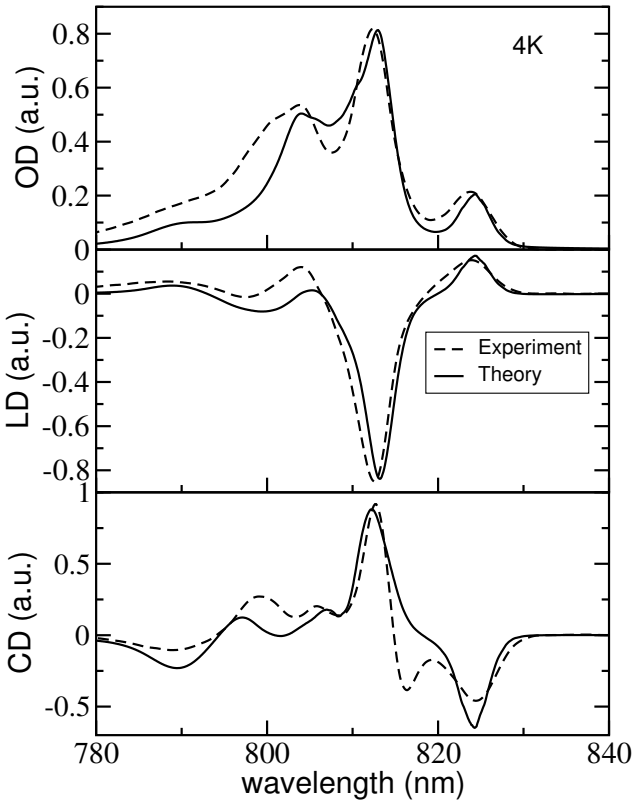

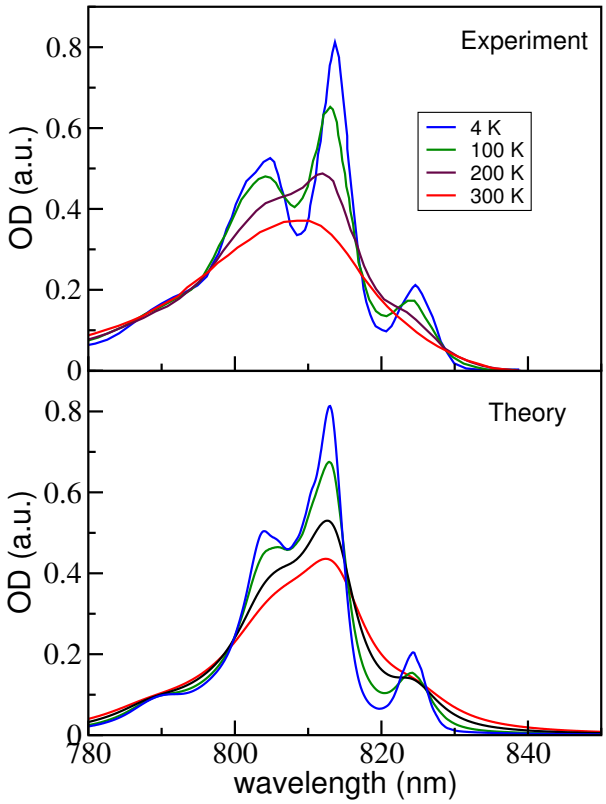

fig. S4. Exciton relaxation in the FMO protein initiated by a δ-pulse excitation. Population dynamics of the exciton states (left) and the local excited states (right) initiated by a δ-pulse excitation at time zero, calculated for room temperature (300 K). The quantum mechanical treatment (eqs. (S11) and (S19)) of the nuclear motion in the upper parts is compared with the classical limit (eq. (S36)) in the lower parts.

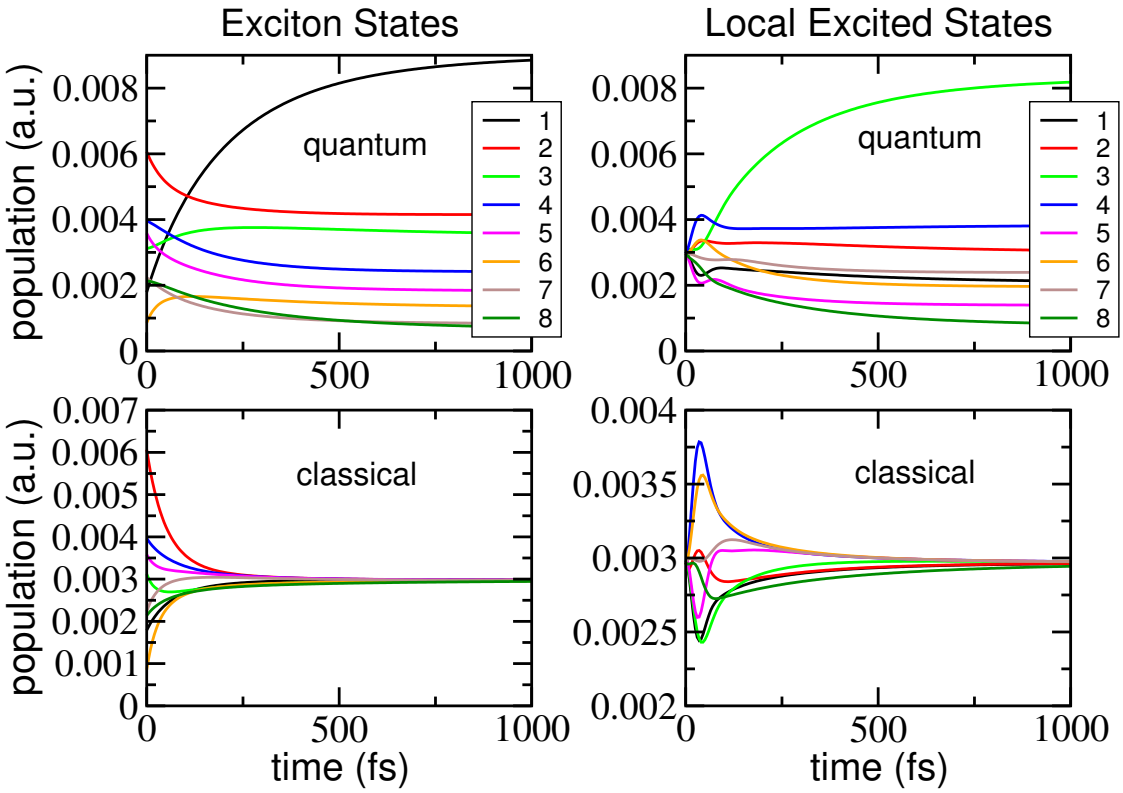

fig. S5. Inter-pigment coherences in the FMO protein. Disorder averaged inter-pigment coherences ρ_{mn} given by eq. (S40) after a δ-pulse excitation at time zero calculated for T = 300 K. The largest equilibrium coherences are labeled as (m, n).

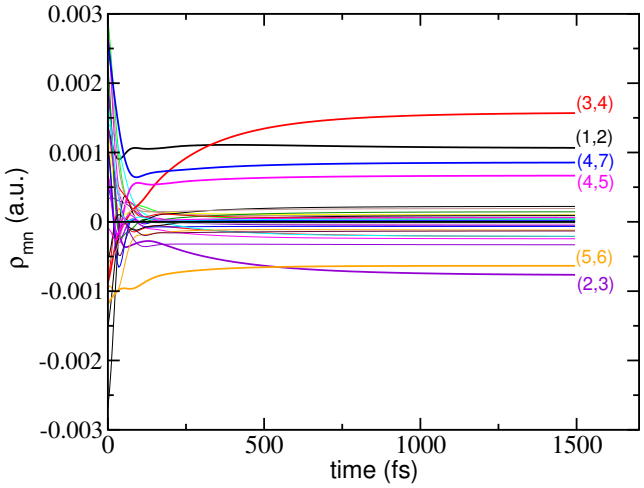

fig. S6. Exciton relaxation in the FMO protein initiated by incoherent transfer from the baseplate. Exciton relaxation in the FMO protein assuming incoherent transfer from the baseplate, as explained in section S5, calculated for room temperature (300 K). A vertical distance R_0 = 20 Å has been assumed between BChl 8 and the baseplate plane. The left half shows exciton state populations and the right part populations of locally excited states of the pigments. The upper and lower parts were obtained using a quantum (eqs. (S11) and (S19)) or classical (eq. (S36)) description, respectively, for the nuclear motion.

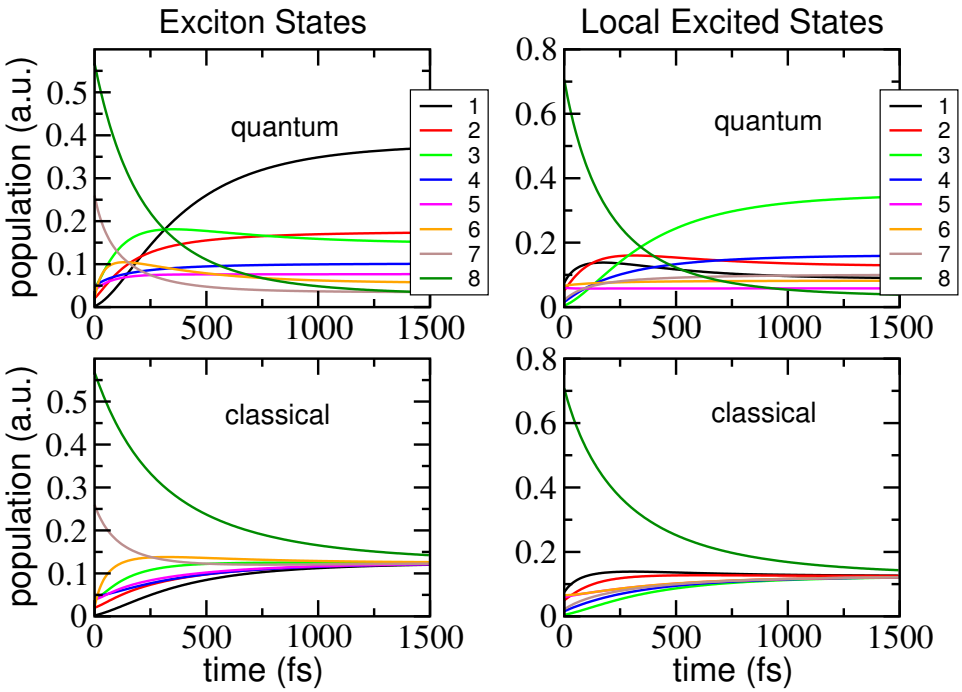

fig. S7. Dependence of the exciton relaxation in the FMO protein on the baseplate excitation energy and distance. Populations of exciton states in the upper left part of Fig. S6 ($\lambda_{\mathrm{BP}} = 805$ nm, $R_0 = 20$ Å) are compared with results obtained for different excitation wavelengths λ_{BP} of the low-energy exciton state of the baseplate (left part) and for different vertical distances R_0 between BChl 8 and the baseplate plane.

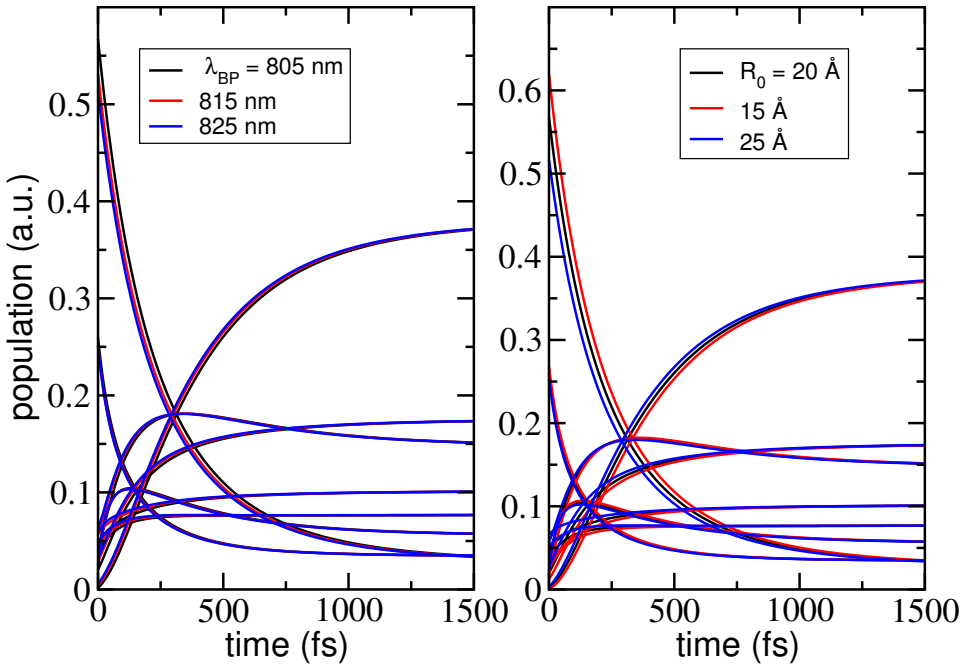

fig. S8. Local population of the excited states in the FMO protein for quantum mechanical and classical treatment of the nuclear motion. Exciton relaxation in the FMO protein assuming incoherent transfer from the baseplate, as in Fig. S6, but illustrating the local populations of excited pigment states at four different times by illuminating the pigments accordingly. Panel a) contains the results obtained by using a quantum description of the nuclear motion (as in Fig. 1 of the main text) and panel b) shows the respective results of the classical calculations.

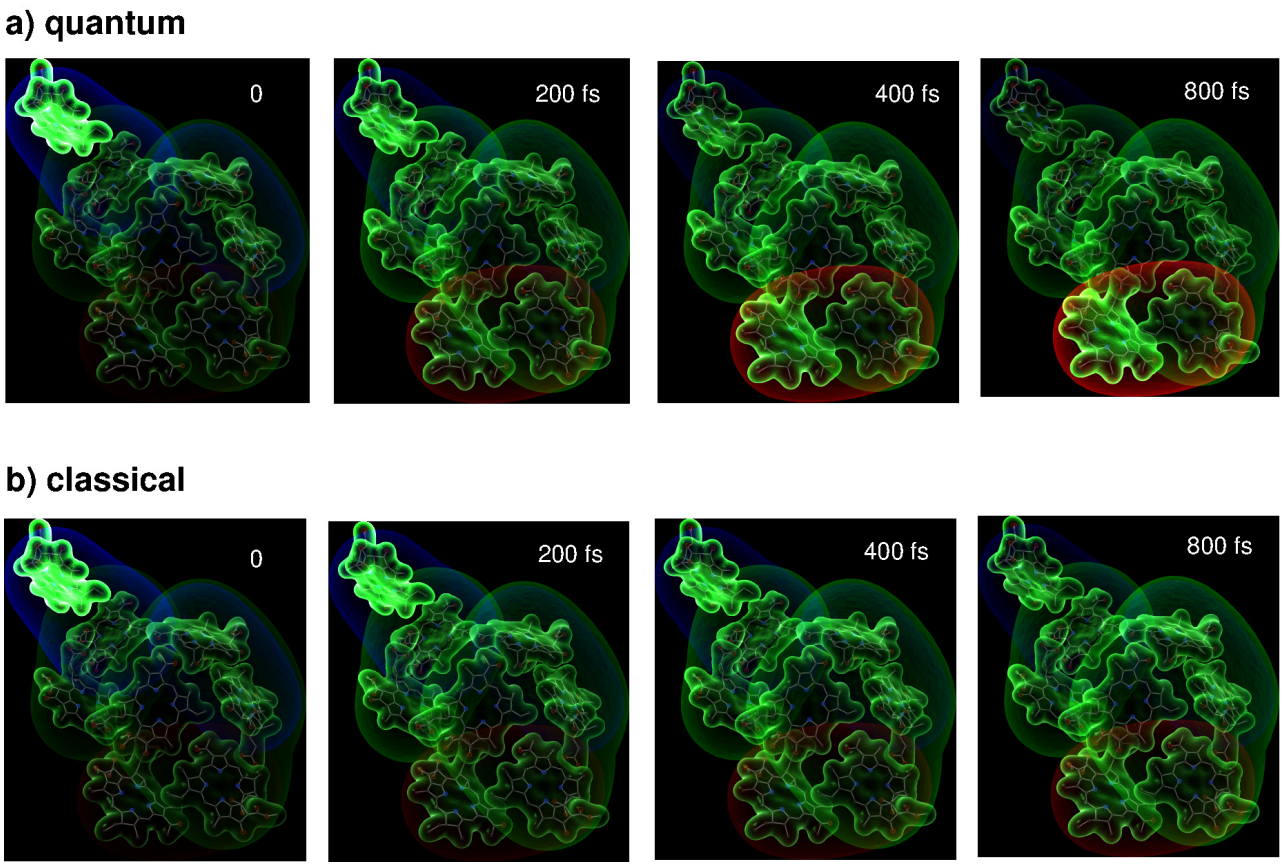

Table S1. Parameters of the Hamiltonian of the FMO protein. Site energies (diagonal) and excitonic couplings (off-diagonal) in holo form of the FMO protein from *P. aestuarii*, all in units of cm^{-1}, according to Ref. (*17*). We note that the excitonic coupling $V_{12} = -94.8$ cm^{-1} in the SI of this reference was misprinted with the wrong sign. The correct sign is given here.

BChl	1	2	3	4	5	6	7	8
1	12505	-94.8	5.5	-5.9	7.1	-15.1	-12.2	39.5
2		12425	29.8	7.6	1.6	13.1	5.7	7.9
3			12195	-58.9	-1.2	-9.3	3.4	1.4
4				12375	-64.1	-17.4	-62.3	-1.6
5					12600	89.5	-4.6	4.4
6						12515	35.1	-9.1
7							12465	-11.1
8								12700

movie S1. Illustration of the exciton relaxation in the FMO protein initiated by incoherent transfer from the baseplate in the presence of a classical bath.

movie S2. Illustration of the exciton relaxation in the FMO protein initiated by incoherent transfer from the baseplate in the presence of a quantum bath.

REFERENCES AND NOTES

1. N. Lambert, Y.-N. Chen, Y.-C. Cheng, C.-M. Li, G.-Y. Chen, F. Nori, Quantum biology. *Nat. Phys.* **9**, 10–18 (2013).
2. J. C. Brookes, Quantum effects in biology: Golden rule in enzymes, olfaction, photosynthesis and magnetodetection. *Proc. Math Phys. Eng. Sci.* **473**, 20160822 (2017).
3. E. Schrödinger, *What is Life?* (Cambridge Univ. Press, Cambridge, 1944).
4. G. S. Engel, T. R. Calhoun, E. L. Read, T.-K. Ahn, T. Mančal, Y.-C. Cheng, R. E. Blankenship, G. R. Fleming, Evidence for wavelike energy transfer through quantum coherence in photosynthetic systems. *Nature* **446**, 782–786 (2007).
5. J. McFadden, J. Al-Khalili, *Life on the Edge: The Coming of Age of Quantum Biology.* (Broadway Books, 2014).
6. S. Mukamel, Comment on "Coherence and uncertainty in nanostructured organic photovoltaics". *J. Phys. Chem. A* **117**, 10563–10564 (2013).
7. V. Sundström, T. Pullerits, R. van Grondelle, Photosynthetic light-harvesting: Reconciling dynamics and structure of purple bacterial LH2 reveals function of photosynthetic unit. *J. Phys. Chem. B* **103**, 2327–2346 (1999).
8. J. Dostál, J. Pšenčík, D. Zigmantas, In situ mapping of the energy flow through the entire photosynthetic apparatus. *Nat. Chem.* **8**, 705–710 (2016).
9. G. Raszewski, T. Renger, Light harvesting in photosystem II core complexes is limited by the transfer to the trap: Can the core complex turn into a photoprotective mode? *J. Am. Chem. Soc.* **130**, 4431–4446 (2008).
10. R. E. Blankenship, *Molecular Mechanisms of Photosynthesis* (Wiley-Blackwell, ed. 2, 2014).
11. R. Croce, R. van Grondelle, H. van Amerogen, I. Van Stokkum, *Light-Harvesting in Photosynthesis* (CRC Press, 2018).
12. H. van Amerongen, R. van Grondelle, L. Valkunas, *Photosynthetic Excitons* (World Scientific, 2000).
13. E. Thyrhaug, K. Žídek, J. Dostál, D. Bína, D. Zigmantas, Exciton structure and energy transfer in the Fenna-Matthews-Olson complex. *J. Phys. Chem. Lett.* **7**, 1653–1660 (2016).
14. D. Abramavicius, B. Palmieri, D. V. Voronine, F. Šanda, S. Mukamel, Coherent multidimensional optical spectroscopy of excitons in molecular aggregates; quasiparticle versus Supermolecule Perspectives. *Chem. Rev.* **109**, 2350–2408 (2009).

15. F. Müh, M. E.-A. Madjet, J. Adolphs, A. Abdurahman, B. Rabenstein, H. Ishikita, E.-W. Knapp, T. Renger, α-helices direct excitation energy flow in the Fenna–Matthews–Olson protein. *Proc. Natl. Acad. Sci. U.S.A.* **104**, 16862–16867 (2007).
16. J. Adolphs, F. Müh, M. E.-A. Madjet, T. Renger, Calculation of pigment transition energies in the FMO protein: From simplicity to complexity and back. *Photosynth. Res.* **95**, 197–209 (2008).
17. M. Schmidt am Busch, F. Müh, M. E.-A. Madjet, T. Renger, The eighth bacteriochlorophyll completes the excitation energy funnel in the FMO protein. *J. Phys. Chem. Lett.* **2**, 93–98 (2011).
18. R. G. Saer, V. Stadnytskyi, N. C. Magdaong, C. Goodson, S. Savikhin, R. E. Blankenship, Probing the excitonic landscape of the *chlorobaculum tepidum* Fenna-Matthews-Olson (FMO) complex: A mutagenesis approach. *Biochim. Biophys. Acta Bioenerg.* **1858**, 288–296 (2017).
19. J. Adolphs, T. Renger, How proteins trigger excitation energy transfer in the FMO complex of green sulfur bacteria. *Biophys. J.* **91**, 2778–2797 (2006).
20. J. Wen, H. Zhang, M. L. Gross, R. E. Blankenship, Membrane orientation of the FMO antenna protein from *chlorobaculum tepidum* as determined by mass spectrometry-based footprinting. *Proc. Natl. Acad. Sci. U.S.A.* **106**, 6134–6139 (2009).
21. J. Moix, J. Wu, P. Huo, D. Coker, J. Cao, Efficient energy transfer in light-harvesting systems, III: The influence of the eighth bacteriochlorophyll on the dynamics and efficiency in FMO. *J. Phys. Chem. Lett.* **2**, 3045–3052 (2011).
22. C. Olbrich, J. Strümpfer, K. Schulten, U. Kleinekathöfer, Theory and simulation of the environmental effects on FMO electronic transitions. *J. Phys. Chem. Lett.* **2**, 1771–1776 (2011).
23. T. Renger, A. Klinger, F. Steinecker, M. Schmidt am Busch, J. Numata, F. Müh, Normal mode analysis of the spectral density of the Fenna-Matthews-Olson Light-Harvesting protein: How the protein dissipates the excess energy of excitons. *J. Phys. Chem. B* **116**, 14565–14580 (2012).
24. S. Chandrasekan, M. Aghtar, S. Valleau, A. Aspuru-Guzik, U. Kleinekathöfer, Influence of force fields and quantum chemistry approach on spectral density of Bchl *a* in solution and in FMO proteins. *J. Phys. Chem. B* **119**, 9995–10004 (2015).

25. E. Rivera, D. Montemayor, M. Masia, D. F. Coker, Influence of site-dependent pigment–Protein interactions on excitation energy transfer in photosynthetic light harvesting. *J. Phys. Chem. B* **117**, 5510–5521 (2013).
26. T. Pullerits, M. Chachisvilis, V. Sundström, Exciton delocalization length in the B850 antenna of *Rhodobacter sphaeroides*. *J. Phys. Chem.* **100**, 10787–10792 (1996).
27. R. Monshouwer, M. Abrahamsson, F. van Mourik, R. van Grondelle, Superradiance and exciton delocalization in bacterial photosynthetic light-harvesting systems. *J. Phys. Chem. B* **37**, 7241–7248 (1997).
28. C. Shane, *An Introduction to Electromagnetic Wave Propagation and Antennas* (Springer Science and Business Media, 1996).
29. T. Mančal, Excitation energy transfer in a classical analogue of photosynthetic antennae. *J. Phys. Chem. B* **117**, 11282–11291 (2013).
30. S. Lee, W. Richter, S. Vathyam, W. S. Warren, Quantum treatment of the effects of dipole-dipole interactions in liquid nuclear magnetic resonance. *J. Chem. Phys.* **105**, 874–900 (1996).
31. J. Jeener, A. Vlassenbroek, P. Broekaert, Unified derivation of the dipolar field and relaxation terms in the Bloch-Redfield equations of liquid NMR. *J. Chem. Phys.* **103**, 1309–1332 (1995).
32. H. Sumi, Theory on rates of excitation-energy transfer between molecular aggregates through distributed transition dipoles with application to the antenna system in bacterial photosynthesis. *J. Phys. Chem. B* **103**, 252–260 (1999).
33. N. Bohr, Über die serienspektra der elemente. *Zeitschrift für Physik* **2**, 423–478 (1920).
34. A. Nitzan, *Chemical Dynamics in the Condensed Phase* (Oxford Univ. Press, 2006).
35. S. J. Cotton, W. H. Miller, The symmetrical quasi-classical model for electronically non-adiabatic processes applied to energy transfer dynamics in site-exciton models of light-harvesting complexes. *J. Chem. Theory Comput.* **12**, 983–991 (2016).
36. H.-D. Meyera, W. H. Miller, A classical analog for electronic degrees of freedom in nonadiabatic collision processes. *J. Chem. Phys.* **70**, 3214–3223 (1979).
37. G. Stock, M. Thoss, Semiclassical description of nonadiabatic quantum dynamics. *Phys. Rev. Lett.* **78**, 578–581 (1997).

38. M. Thoss, G. Stock, Mapping approach to the semiclassical description of nonadiabatic quantum dynamics. *Phys. Rev. A* **59**, 64–79 (1999).
39. R. Tempelaar, T. L. C. Jansen, J. Knoester, Vibrational beatings conceal evidence of electronic coherence in the FMO light-harvesting complex. *J. Phys. Chem. B* **118**, 12865–12872 (2014).
40. N. Makri, D. E. Makarov, Tensor propagator for iterative quantum time evolution of reduced density matrices. I. Theory. *J. Chem. Phys.* **102**, 4600–4610 (1995).
41. N. Makri, D. E. Makarov, Tensor propagator for iterative quantum time evolution of reduced density matrices. II. Numerical methodology. *J. Chem. Phys.* **102**, 4611–4618 (1995).
42. P. Nalbach, D. Braun, M. Thorwart, Exciton transfer dynamics and quantumness of energy transfer in the Fenna-Matthews-Olson complex. *Phys. Rev. E Stat. Nonlin. Soft Matter Phys.* **84**, 041926 (2011).
43. C. A. Mujica-Martinez, P. Nalbach, M. Thorwart, Quantification of non-Markovian effects in the Fenna-Matthews-Olson complex. *Phys. Rev. E Stat. Nonlin. Soft Matter Phys.* **88**, 062719 (2013).
44. P. Nalbach, C. A. Mujica-Martinez, M. Thorwart, Vibronically coherent speed-up of the excitation energy transfer in the Fenna–Matthews–Olson complex. *Phys. Rev. E Stat. Nonlin. Soft Matter Phys.* **91**, 022706 (2015).
45. Y. Tanimura, R. Kubo, Time evolution of quantum system in contact with a nearly Gaussian-Markovian noise bath. *J. Phys. Soc. Jpn.* **58**, 101–114 (1989).
46. J. S. Bader, B. J. Berne, Quantum and classical relaxation rates from classical simulations. *J. Chem. Phys.* **100**, 8359–8366 (1994).
47. S. A. Egorov, E. Rabani, B. J. Berne, Vibronic spectra in condensed matter: A comparison of exact quantum mechanical and various semiclassical treatments for harmonic baths. *J. Chem. Phys.* **108**, 1407–1422 (1998).
48. W.H. Miller, Perspective: Quantum or classical coherence? *J. Chem. Phys.* **136**, 210901 (2012).
49. J. S. Briggs, A. Eisfeld, Equivalence of quantum and classical coherence in electronic energy transfer. *Phys. Rev. E Stat. Nonlin. Soft Matter Phys.* **83**, 051911 (2011).
50. E. N. Zimanyi, R. J. Silbey, Unified treatment of coherent and incoherent electronic energy transfer dynamics using classical electrodynamics. *J. Chem. Phys.* **133**, 144107 (2010).

51. S. Mukamel, Communications: Signature of quasiparticle entanglement in multidimensional nonlinear optical spectroscopy of aggregates. *J. Chem. Phys.* **132**, 241105 (2010).
52. M. Reppert, P. Brumer, Quantumness in light harvesting is determined by vibrational dynamics. *J. Chem. Phys.* **149**, 234102 (2018).
53. U. Weiss, *Quantum Dissipative Systems* (World Scientific, Singapore, ed. 3, 2008).
54. R. P. Feynman, F. L. Vernon Jr., The theory of a general quantum system interacting with a linear dissipative system. *Ann. Phys-New York* **24**, 118–173 (1963).
55. A. W. Chin, A. Rivas, S. F. Huelga, M. B. Plenio, Exact mapping between system-reservoir quantum models and semi-infinite discrete chains using orthogonal polynomials. *J. Math. Phys.* **51**, 092109 (2010).
56. P. Huo, D. F. Coker, Iterative linearized density matrix propagation for modeling coherent excitation energy transfer in photosynthetic light harvesting. *J. Chem. Phys.* **133**, 184108 (2010).
57. J. M. Moix, J. Ma, J. Cao, Förster reson0061nce energy transfer, absorption and emission spectra in multichromophoric systems. III. Exact stochastic path integral evaluation. *J. Chem. Phys.* **142**, 094108 (2015).
58. Y. Tanimura, Reduced hierarchy equation of motion approach with Drude plus Brownian spectral distribution: Probing electron transfer processes by means of two-dimensional correlation spectroscopy. *J. Chem. Phys.* **137**, 22A550 (2012).
59. H. Lee, Y.-C. Cheng, G. R. Fleming, Coherence dynamics in photosynthesis: protein protection of excitonic coherence. *Science* **316**, 1462–1465 (2007).
60. A. W. Chin, S. F. Huelga, M. B. Plenio, Coherence and decoherence in biological systems: Principles of noise-assisted transport and the origin of long-lived coherences. *Philos. Trans. A Math Phys. Eng. Sci.* **370**, 3638–3657 (2012).
61. B. S. Rolczynski, H. Zheng, V. P. Singh, P. Navotnaya, A. R. Ginzburg, J. R. Caram, K. Ashraf, A. T. Gardiner, S.-H. Yeh, S. Kais, R. J. Cogdell, G. S. Engel, Correlated protein environments drive quantum coherence lifetimes in photosynthetic pigment-protein complexes. *Chem* **4**, 138–149 (2018).
62. P. Brumer, M. Shapiro, Molecular response in one-photon absorption via natural thermal light vs. pulsed laser excitation. *Proc. Natl. Acad. Sci. U.S.A.* **109**, 19575–19578 (2012).

63. T. Mančal, L. Valkunas, Exciton dynamics in photosynthetic complexes: Excitation by coherent and incoherent light. *New J. Phys.* **12**, 065044 (2010).
64. J. Olšina, A. G. Dijkstra, C. Wang, J. Cao, Can natural sunlight induce coherent exciton dynamics? arXiv:1408.5385 (2014).
65. H. C. H. Chan, O. E. Gamel, G. R. Fleming, K. B. Whaley, Single-photon absorption by single photosynthetic light-harvesting complexes. *J. Phys. B At. Mol. Opt. Phys.* **51**, 054002 (2018).
66. F. Müh, M. Plöckinger, T. Renger, Electrostatic asymmetry in the Reaction Center of Photosystem II. *J. Phys. Chem. Lett.* **8**, 850–858 (2017).
67. V. Butkus, D. Zigmantas, L. Valkunas, D. Abramavicius, Vibrational vs. electronic coherences in 2D spectrum of molecular systems. *Chem. Phys. Lett.* **545**, 40–43 (2012).
68. H.-G. Duan, P. Nalbach, V. I. Prokhorenko, S. Mukamel, M. Thorwart, On the origin of oscillations in two-dimensional spectra of excitonically-coupled molecular systems. *New J. Phys.* **17**, 072002 (2015).
69. A. Halpin, P. J. M. Johnson, R. Tempelaar, R. S. Murphy, J. Knoester, T. L. C. Jansen, R. J. D. Miller, Two-dimensional spectroscopy of a molecular dimer unveils the effects of vibronic coupling on exciton coherences. *Nat. Chem.* **6**, 196–201 (2014).
70. C. Aslangul, P. Kottis, Density operator description of excitons in molecular aggregates: Optical absorption and motion. I. The dimer problem. *Phys. Rev. B* **10**, 4364–4382 (1974).
71. L. Wang, M. A. Allodi, G. S. Engel, Quantum coherences reveal excited-state dynamics in biophysical systems. *Nat. Rev. Chem.* **3**, 477–490 (2019).
72. Y.-C. Cheng, G. R. Fleming, Coherence quantum beats in two-dimensional electronic spectroscopy. *J. Phys. Chem. A* **112**, 4254–4260 (2008).
73. A. Nemeth, F. Milota, T. Mančal, V. Lukeš, J. Hauer, H. F. Kauffmann, J. Sperling, Vibrational wave packet induced oscillations in two-dimensional electronic spectra. I. Experiments. *J. Chem. Phys.* **132**, 184514 (2010).
74. T. Mančal, A. Nemeth, F. Milota, V. Lukeš, H. F. Kauffmann, J. Sperling, Vibrational wave packet induced oscillations in two-dimensional electronic spectra. II. Theory. *J. Chem. Phys.* **132**, 184515 (2010).
75. J. Dostál, T. Mančal, F. Vácha, J. Pšenčík, D. Zigmantas, Unraveling the nature of coherent beatings in chlorosomes. *J. Chem. Phys.* **140**, 115103 (2014).

76. V. Butkus, D. Zigmantas, D. Abramavicius, L. Valkunas, Distinctive character of electronic and vibrational coherences in disordered molecular aggregates. *Chem. Phys. Lett.* **587**, 93–98 (2013).
77. T. Mančal, N. Christensson, V. Lukeš, F. Milota, O. Bixner, H. F. Kauffmann, J. Hauer, System-dependent signatures of electronic and vibrational coherences in electronic two-dimensional spectra. *J. Phys. Chem. Lett.* **3**, 1497–1502 (2012).
78. S. Yue, Z. Wang, X. Leng, R.-D. Zhu, H.-L. Chen, Y.-X. Weng, Coupling of multi-vibrational modes in bacteriochlorophyll *a* in solution observed with 2D electronic spectroscopy. *Chem. Phys. Lett.* **683**, 591–597 (2017).
79. E. Collini, C. Y. Wong, K. E. Wilk, P. M. G. Curmi, P. Brumer, G. D. Scholes, Coherently wired light-harvesting in photosynthetic marine algae at ambient temperature. *Nature* **463**, 644–647 (2010).
80. E. Harel, G. S. Engel, Quantum coherence spectroscopy reveals complex dynamics in bacterial light-harvesting complex 2 (LH2). *Proc. Natl. Acad. Sci. U.S.A.* **109**, 706–711 (2012).
81. T. Brixner, J. Stenger, H. M. Vaswani, M. Cho, R. E. Blankenship, G. R. Fleming, Two-dimensional spectroscopy of electronic couplings in photosynthesis. *Nature* **434**, 625–628 (2005).
82. D. Zigmantas, E. L. Read, T. Mančal, T. Brixner, A. T. Gardiner, R. J. Cogdell, G. R. Fleming, Two-dimensional electronic spectroscopy of the B800-B820 light-harvesting complex. *Proc. Natl. Acad. Sci. U.S.A.* **103**, 12672–12677 (2006).
83. M. H. Vos, J. C. Lambry, S. J. Robles, D. C. Youvan, J. Breton, J. L. Martin, Direct observation of vibrational coherence in bacterial reaction centers using femtosecond absorption-spectroscopy. *Proc. Natl. Acad. Sci. U.S.A.* **88**, 8885–8889 (1991).
84. M. H. Vos, F. Rappaport, J.-C. Lambry, J. Breton, J.-L. Martin, Visualization of coherent nuclear motion in a membrane-protein by femtosecond spectroscopy. *Nature* **363**, 320–325 (1993).
85. M. Chachisvilis, T. Pullerits, M. R. Jones, C. N. Hunter, V. Sundström, Vibrational dynamics in the light-harvesting complexes of the photosynthetic bacterium *Rhodobacter sphaeroides*. *Chem. Phys. Lett.* **224**, 345–354 (1994).

86. S. Savikhin, D. R. Buck, W. S. Struve, Oscillating anisotropies in a bacteriochlorophyll protein: Evidence for quantum beating between exciton levels. *Chem. Phys.* **223**, 303–312 (1997).
87. G. S. Schlau-Cohen, A. Ishizaki, T. R. Calhoun, N. S. Ginsberg, M. Ballottari, R. Bassi, G. R. Fleming, Elucidation of the timescales and origin of quantum electronic coherence in LHCII. *Nat. Chem.* **4**, 389–395 (2012).
88. G. Panitchayangkoon, D. Hayes, K. A. Fransted, J. R. Caram, E. Harel, J. Wen, R. E. Blankenship, G. S. Engel, Long-lived quantum coherence in photosynthetic complexes at physiological temperature. *Proc. Natl. Acad. Sci. U.S.A.* **107**, 12766–12770 (2010).
89. D. Paleček, P. Edlund, S. Westenhoff, D. Zigmantas, Quantum coherence as a witness of vibronically hot energy transfer in bacterial reaction center. *Sci. Adv.* **3**, e1603141 (2017).
90. H.-G. Duan, V. I. Prokhorenko, R. J. Cogdell, K. Ashraf, A. L. Stevens, M. Thorwart, R. J. D. Miller, Nature does not rely on long-lived electronic quantum coherence for photosynthetic energy transfer. *Proc. Natl. Acad. Sci. U.S.A.* **114**, 8493–8498 (2017).
91. M. Maiuri, E. E. Ostroumov, R. G. Saer, R. E. Blankenship, G. D. Scholes, Coherent wavepackets in the Fenna-Matthews-Olson complex are robust to excitonic-structure perturbations caused by mutagenesis. *Nat. Chem.* **10**, 177–183 (2018).
92. E. Thyrhaug, R. Tempelaar, M. J. P. Alcocer, K. Žídek, D. Bína, J. Knoester, T. L. C. Jansen, D. Zigmantas, Identification and characterization of diverse coherences in the Fenna-Matthews-Olson complex. *Nat. Chem.* **10**, 780–786 (2018).
93. V. R. Policht, A. Niedringhaus, J. P. Ogilvie, Characterization of vibrational coherence in monomeric bacteriochlorophyll a by two-dimensional electronic spectroscopy. *J. Phys. Chem. Lett.* **9**, 6631–6637 (2018).
94. H.-G. Duan, A. L. Stevens, P. Nalbach, M. Thorwart, V. I. Prokhorenko, R. J. D. Miller, Two-dimensional electronic spectroscopy of light-harvesting complex II at ambient temperature: A joint experimental and theoretical study. *J. Phys. Chem. B* **119**, 12017–12027 (2015).
95. H.-G. Duan, V. I. Prokhorenko, E. Wientjes, R. Croce, M. Thorwart, R. J. D. Miller, Primary charge separation in the Photosystem II reaction center revealed by a Global Analysis of the two-dimensional electronic spectra. *Sci. Rep.* **7**, 12347 (2017).

96. V. Tiwari, W. K. Peters, D. M. Jonas, Electronic resonance with anticorrelated pigment vibrations drives photosynthetic energy transfer outside the adiabatic framework. *Proc. Natl. Acad. Sci. U.S.A.* **110**, 1203–1208 (2013).
97. N. Christensson, H. F. Kauffmann, T. Pullerits, T. Mančal, Origin of long-lived coherences in light-harvesting complexes. *J. Phys. Chem. B* **116,** 7449–7454 (2012).
98. J. M. Womick, A. M. Moran, Vibronic enhancement of exciton sizes and energy transport in photosynthetic complexes. *J. Phys. Chem. B* **115**, 1347–1356 (2011).
99. F. D. Fuller, J. Pan, A. Gelzinis, V. Butkus, S. S. Senlik, D. E. Wilcox, C. F. Yocum, L. Valkunas, D. Abramavicius, J. P. Ogilvie, Vibronic coherence in oxygenic photosynthesis. *Nat. Chem.* **6**, 706–711 (2014).
100. E. Romero, R. Augulis, V. I. Novoderezhkin, M. Ferretti, J. Thieme, D. Zigmantas, R. van Grondelle, Quantum coherence in photosynthesis for efficient solar-energy conversion. *Nat. Phys.* **10**, 676–682 (2014).
101. S.-H. Yeh, R. D. Hoehn, M. A. Allodi, G. S. Engel, S. Kais, Elucidation of near-resonance vibronic coherence lifetimes by nonadiabatic electronic-vibrational state character mixing. *Proc. Natl. Acad. Sci. U.S.A.* **116**, 18263–18268 (2019).
102. H.-G. Duan, M. Thorwart, R. J. D. Miller, Does electronic coherence enhance anticorrelated pigment vibrations under realistic conditions? *J. Chem. Phys.* **151**, 114115 (2019).
103. X.-P. Jiang, P. Brumer, Creation and dynamics of molecular states prepared with coherent vs partially coherent pulsed light. *J. Chem. Phys.* **94**, 5833–5843 (1991).
104. T. Renger, R. A. Marcus, On the relation of protein dynamics and exciton relaxation in pigment-protein complexes: An estimation of the spectral density and a theory for the calculation of optical spectra. *J. Chem. Phys.* **116**, 9997–10019 (2002).
105. M. Wendling, T. Pullerits, M. A. Przyjalgowski, S. I. E. Vulto, T. J. Aartsma, R. van Grondelle, H. van Amerongen**,** Electron-vibrational coupling in the Fenna-Matthews-Olson complex of *Prosthecochloris aestuarii* determined by temperature-dependent absorption and fluorescence line-narrowing measurements. *J. Phys. Chem. B* **104**, 5825–5831 (2000).
106. D. E. Tronrud, J. Wen, L. Gay, R. E. Blankenship, The structural basis for the difference in absorbance spectra for the FMO antenna protein from various green sulfur bacteria. *Photosynth. Res.* **100**, 79–87 (2009).

107. J. Adolphs, F. Maier, T. Renger, Wavelength-dependent exciton-vibrational coupling in the water-soluble chlorophyll binding protein revealed by multilevel theory of difference fluorescence line-narrowing. *J. Phys. Chem. B* **122**, 8891–8899 (2018).

108. B. Hein, C. Kreisbeck, T. Kramer, M. Rodríguez, Modelling of oscillation in two-dimensional echo-spectra of the Fenna–Matthews–Olson complex. *New J. Phys.* **14**, 023018 (2012).

109. T.-C. Dinh, T. Renger, Towards an exact theory of linear absorbance and circular dichroism of pigment-protein complexes: Importance of non-secular contribution. *J. Chem. Phys.* **142**, 034104 (2015).

110. J. Ma, J. Cao, Förster resonance energy transfer, absorption and emission spectra in multichromophoric systems. I. Full cumulant expansions and system-bath entanglement. *J. Chem. Phys.* **142**, 094106 (2015).

111. M. Wendling, M. A. Przyjalgowski, D. Gülen, S. I. E. Vulto, T. J. Aartsma, R. van Grondelle, H. van Amerongen, The quantitative relationship between structure and polarized spectroscopy in the FMO complex of *Prosthecochloris aestuarii*: Refining experiments and simulations. *Photosynth. Res.* **71**, 99–123 (2002).

112. G. Raszewski, W. Saenger, T. Renger, Theory of optical spectra of photosystem II reaction centers: Location of the triplet state and the identity of the primary electron donor. *Biophys. J.* **88**, 986–998 (2005).

113. P. V. Parendekar, J. C. Tully, Mixed quantum-classical equilibrium. *J. Chem. Phys.* **122**, 094102 (2005).

114. W. H. Miller, S. J. Cotton, Communication: Note on detailed balance in symmetrical quasi-classical models for electronically non-adiabatic dynamics. *J. Chem. Phys.* **142**, 131103 (2015).

115. D. Lindorfer, T. Renger, Theory of anisotropic circular dichroism of excitonically coupled systems: Application to the baseplate of green sulfur bacteria. *J. Phys. Chem. B* **122**, 2747–2756 (2018).

116. M. Lax, The Franck-condon principle and its application to crystals. *J. Chem. Phys.* **20**, 1752–1760 (1952).

117. J. Dostál, F. Vácha, J. Pšenčík, D. Zigmantas, 2D electronic spectroscopy reveals excitonic structure in the baseplate of a chlorosome. *J. Phys. Chem. Lett.* **5**, 1743–1747 (2014).